iScience

CellPress
OPEN ACCESS

Article

Photogeneration of singlet oxygen catalyzed by hexafluoroisopropanol for selective degradation of dyes

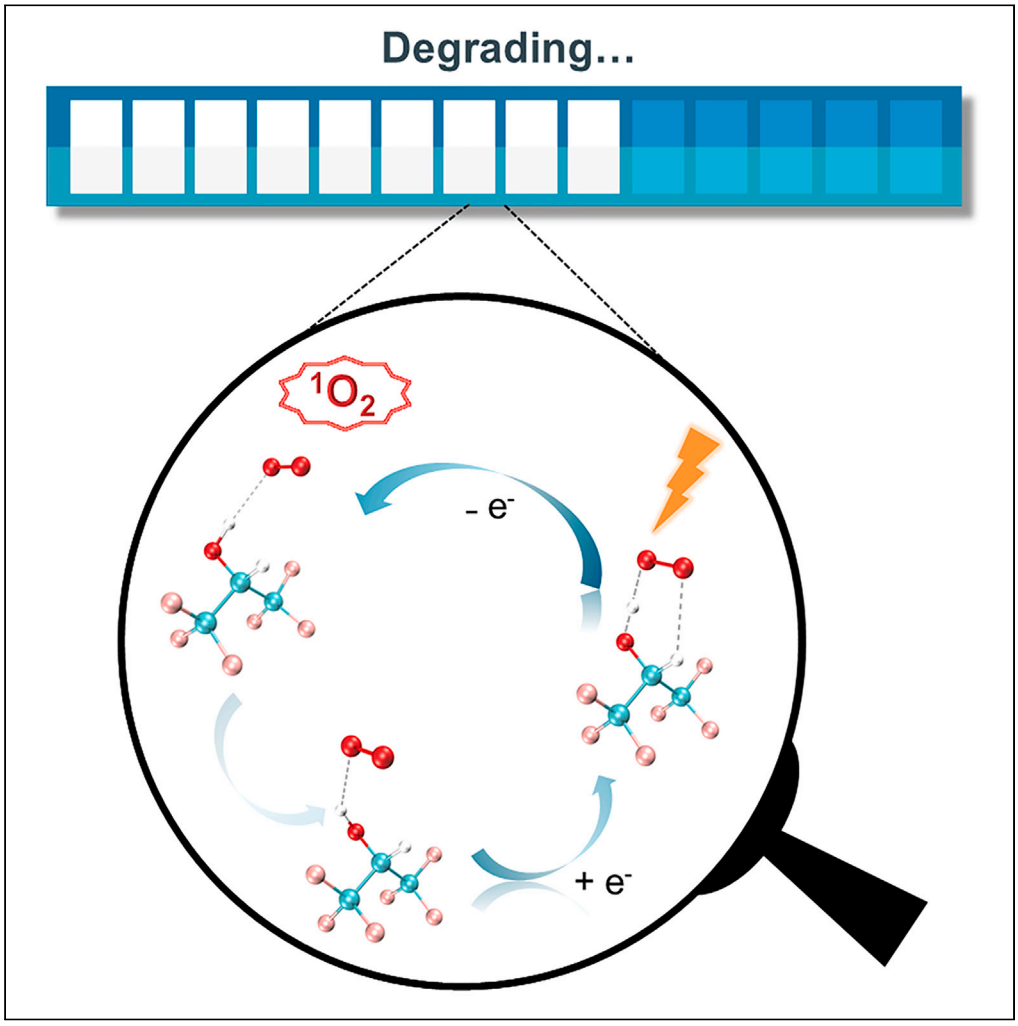

Jia Han, Lei Wang, Wenjin Cao, Qinqin Yuan, Xiaoguo Zhou, Shilin Liu, Xue-Bin Wang

xzhou@ustc.edu.cn (X.Z.)
xuebin.wang@pnnl.gov (X.-B.W.)

Highlights

A novel methodology for photogeneration of singlet oxygen catalyzed by HFIP anion

A catalytic cycle upon electron injection and UV irradiation for dye degradation

The molecular mechanisms for the photogeneration of singlet oxygen are revealed

Han et al., iScience 26, 107306
August 18, 2023
https://doi.org/10.1016/j.isci.2023.107306

iScience

CellPress
OPEN ACCESS

Article

Photogeneration of singlet oxygen catalyzed by hexafluoroisopropanol for selective degradation of dyes

Jia Han,[1] Lei Wang,[1] Wenjin Cao,[2] Qinqin Yuan,[3] Xiaoguo Zhou,[1,4,*] Shilin Liu,[1] and Xue-Bin Wang[2,*]

SUMMARY

Singlet oxygen ($^1O_2$) shows great potential for selective degradation of dyes in environmental remediation of wastewater. In this study, we showcased that $^1O_2$ can be effectively generated from an anion complex composed of deprotonated hexafluoroisopropanol anion ($[HFIP_{-H}]^-$) with hydroperoxyl radical ($\cdot HO_2$) via ultraviolet (UV) photodetachment. Electronic structure calculations and cryogenic negative ion photoelectron spectroscopy unveil critical proton transfer upon complex formation and electron ejection, effectively photoconverting prevalent triplet ground state $^3O_2$ to long-lived excited $^1O_2$, stabilized by nearby HFIP. Inspired by this spectroscopic study, a novel "photogeneration" strategy is proposed to produce $^1O_2$ with the incorporation of atmospheric O_2 and HFIP, acting as a catalyst. Conceptually, the designed catalytic cycle upon UV irradiation and electron injection is able to achieve different degradations of dye molecules in a controllable fashion from decolorization to complete mineralization, shedding new light on potential water purification.

INTRODUCTION

As a highly reactive oxidant with electrophilic nature, singlet oxygen ($^1O_2$) is known to selectively undergo reactions with a wide range of unsaturated organics via electrophilic addition and electron abstraction.[1] Owing to its selectivity toward electron-rich organic compounds, the vital role of $^1O_2$ has been reported for efficient treatments of water contaminants, especially in the degradation of synthetic dyes typically functionalized with electron-donating groups.[2–8] A Fenton-like reaction system with $^1O_2$ as an exclusive reactive intermediate was discovered to exhibit remarkable degradation activity toward a model pollutant methylene blue.[9] Similarly, a complete oxidation of rhodamine B was observed to proceed with $^1O_2$-mediated nonradical pathway identified in the catalytic activation of peroxydisulfate over manganese oxides.[10] Nonradical oxidation mechanism dominated by $^1O_2$ shows apparent superiorities over radical-based processes that include enhanced degradation efficiency due to strong resistance to nontarget background substances in complex water matrixes, intrinsic avoidance of undesired radical self-quenching, and an effective inhibition on the production of halide carcinogenic byproducts.[11–16]

Generation of $^1O_2$ is therefore of great importance regarding its promising applications in textile wastewater treatment. Advanced oxidation processes (AOPs) involving persulfates activated by metal-based or carbon-based catalysts have been reported being effective to generate $^1O_2$.[14,17–21] However, secondary pollutions caused by inevitable metal leaching into environment and high costs originating from complicated synthesis routes for carbon materials confine their applications in actual remediation of contaminated water matrix.[15] The exploitation of photons which can be considered as the cleanest chemical reagent reduces the risk of secondary pollutions and makes additional treatments unnecessary.[22] Dye-sensitized photocatalysis based on photosensitization effect where the dye serves as both a sensitizer and a substrate to be degraded shows prospect of generating $^1O_2$ via energy transfer pathway without introducing any dopants or surface modifications.[23–26] However, irreversible oxidation of absorbed dye molecules by produced active species leads to decolorization under prolonged illumination, destruction of chromophore structures, and prohibiting further photoactivity.[27] An alternative strategy for generating $^1O_2$ in a controllable manner is therefore being actively pursued, ultimately aiming to complete decomposition of dyes to carbon dioxide and water, or partial degradation into lower molecular weight species as a preliminary treatment for subsequent bioprocessing.

[1]Hefei National Laboratory for Physical Sciences at the Microscale, Department of Chemical Physics, University of Science and Technology of China, Hefei, Anhui 230026, P.R. China

[2]Physical Sciences Division, Pacific Northwest National Laboratory, Richland, WA 99352, USA

[3]Department of Chemistry, Anhui University, Hefei, Anhui 230601, P.R. China

[4]Lead contact

*Correspondence: xzhou@ustc.edu.cn (X.Z.), xuebin.wang@pnnl.gov (X.-B.W.)

https://doi.org/10.1016/j.isci.2023.107306

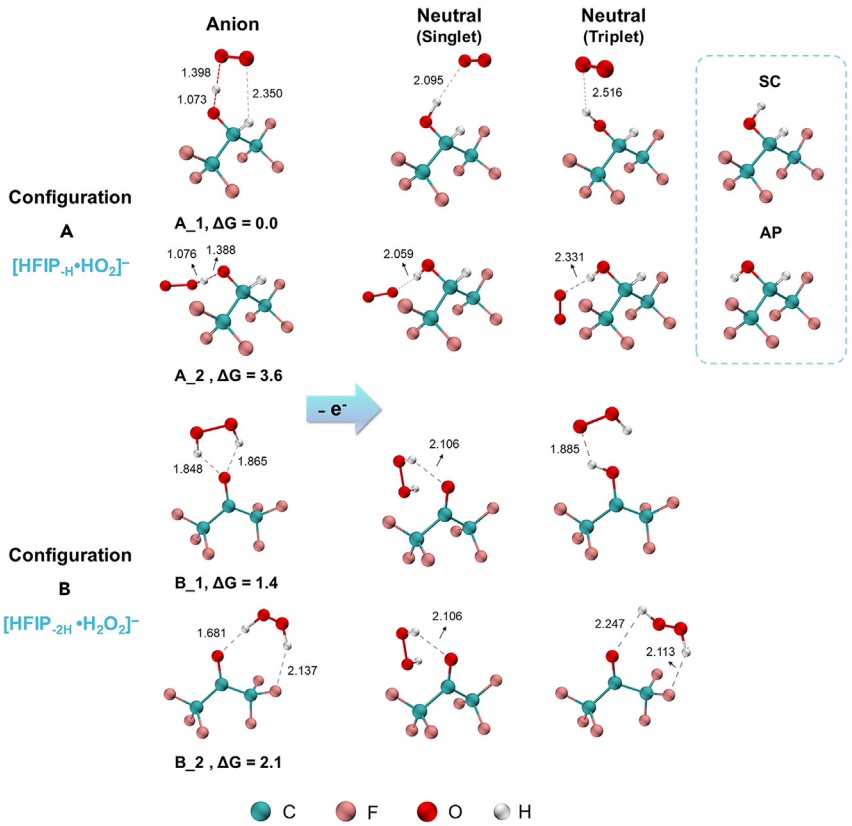

Figure 1. Low-lying structures of anion complexes for both configurations

(A and B) Low-lying, ωB97XD/jun-cc-pVTZ optimized isomers for configuration (A) $[HFIP_{-H}•HO_2]^-$ and configuration (B) $[HFIP_{-2H}•H_2O_2]^-$ complex anions and their corresponding neutral counterparts. Hydrogen bond lengths (in Å) and DLPNO-CCSD(T)/aug-cc-pVTZ//ωB97XD/jun-cc-pVTZ Gibbs free energies (at 300 K) relative to the most stable structure A_1 (ΔG, in kcal/mol) are noted. The inset compares SC and AP conformers of HFIP.

Herein, a novel approach to directly photogenerate $^1O_2$ *in situ* is proposed with perspective for selective oxidation of synthetic dyes in the context of wastewater treatment. Under the synergistic cooperation of electron attachment and UV irradiation, atmospheric O_2 complexed with hexafluoroisopropanol (HFIP) exhibits as a potent molecular system with the ability to produce $^1O_2$, in which HFIP acts as an ideal catalyst owing to its outstanding properties to stabilize ionic species as a strong hydrogen-bond donor and to endure powerful oxidizing conditions endowed with the presence of electron-withdrawing trifluoromethyl groups.[28–30] Negative ion photoelectron spectroscopy (NIPES) combined with high-level quantum chemistry calculations were carried out to investigate the intrinsic molecular properties of complex anions and formed neutrals. The obtained information on the geometrical and electronic structures of the detected species provides a molecular-level basis to decipher the underlying mechanism in a complete catalytic cycle that opens a new avenue for effective photogeneration of $^1O_2$.

RESULTS

Photogeneration of singlet oxygen

The targeted $[HFIP_{-H}•HO_2]^-$ and/or $[HFIP_{-2H}•H_2O_2]^-$ complex anions are synthesized by electrospray ionization (ESI, an ideal soft ionization interface capable of fetching pristine ionic species and aggregates from solutions) and subsequently transferred to the gas phase for mass selection and spectroscopic scrutinization in vacuum without any environmental perturbations. Low-lying structures of anion complexes for both $[HFIP_{-H}•HO_2]^-$ and $[HFIP_{-2H}•H_2O_2]^-$ configurations are identified, and their relative Gibbs free energy are calculated (Figure 1). In the case of $[HFIP_{-H}•HO_2]^-$ denoted as configuration A, the global minimum A_1 features a dual hydrogen bond network within the $[HFIP_{-H}]^-$ symmetry plane, comprising a strong O–H•••O interaction and a weak C–H•••O hydrogen bond, thereby providing a remarkable stabilization

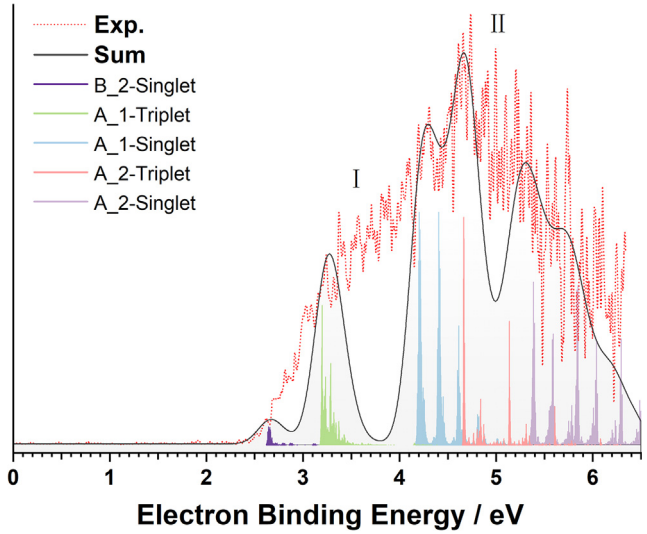

Figure 2. Twenty Kelvin negative ion photoelectron spectrum of $[HFIP_{-H}\cdot HO_2]^-$ and/or $[HFIP_{-2H}\cdot H_2O_2]^-$ complex anions at 193 nm (6.424 eV) (dotted red) and simulated NIPE spectrum (gray) using the calculated stick spectra (violet for the transitions of B_2 to its singlet neutral state; green and blue for transitions of A_1 to the neutral triplet and singlet states; pink and light violet for transitions of A_2 to the neutral triplet and singlet states) convoluted with Gaussian line broadening (the FWHM was set to 300 meV). The simulated spectrum for each low-lying structure compared with the experimental spectrum is provided in Figure S3.

for this anion complex. Noting a partial hydrogen relocation occurs from HO_2 to $HFIP_{-H}$ moiety upon complexing as evidenced by an apparent increase of the O–H bond length in the HO_2 part, resulting in a binding motif more reasonable to classify as $[HFIP\cdot O_2]^-$. However, we hereby remain its designation representing original components to be consistent and avoid any confusion in discussions. Isomer A_2 adopts a different relative orientation to form a single O–H•••O hydrogen bond, calculated to be higher in free energy than A_1 by 3.6 kcal/mol. Other high-lying isomers are excluded in the following discussions due to their significantly higher energies that render them inaccessible under ambient conditions. The second category B, $[HFIP_{-2H}\cdot H_2O_2]^-$ anion complexes, are all characterized by two hydrogen bonds. The energetically lowest-lying isomer B_1 is composed of *cis*-H_2O_2 and $HFIP_{-2H}^{\bullet -}$ radical anion (namely hexafluoroacetone $[HFA]^{\bullet -}$ in a geometry resembling its gaseous free structure) with two hydrogen bonds formed between two H atoms of *cis*-H_2O_2 and the O atom of $HFA^{\bullet -}$. This structure lies 1.4 kcal/mol higher in energy above A_1. The second low-lying isomer, B_2, contains a typical O–H•••O hydrogen bond together with a weaker O–H•••F interaction, which are less stable than B_1 by 0.7 kcal/mol (see Tables S1 and S2).

Starting from each anion geometry, the corresponding neutral structures in both singlet and triplet states are optimized as well (Figure 1). When an electron is photodetached from A_1, the O–H distance between the O atom of $HFIP_{-H}$ and the relocated H atom of HO_2 further decreases to 0.962 and 0.959 Å in the respective singlet and triplet neutral complex. The formation of a typical O–H covalent bond indicates a complete proton transfer from the HO_2 to $HFIP_{-H}$, leading to a new binding configuration as O_2 molecule is weakly attached to HFIP in synclinal (*SC*) conformation. In a similar manner, a proton transfer from HO_2 side to $HFIP_{-H}$ moiety takes place upon electron removal from A_2, producing $HFIP\cdot O_2$ complex with HFIP in antiperiplanar (*AP*) structure for both singlet and triplet states (see the inset for the comparison between *SC* and *AP*). For configuration B_1 and B_2, electronic transitions from anionic ground states to neutral singlet states all induce large H_2O_2 twisting motions and converge to the same geometry. By comparison, a proton transfer is predicted to occur from H_2O_2 to $HFIP_{-2H}$, giving rise to neutral triplet complex $HFIP_{-H}\cdot HO_2$ from B_1. Different structural changes are observed in optimizing the triplet neutral state from B_2, with two hydrogen bonds remaining intact albeit becoming considerably weaker.

UV photons are applied to generate $^1O_2$ from the target anion complexes by means of electron photodetachment and the resulting negative ion photoelectron (NIPE) spectrum reveals the intrinsic electronic transition mechanisms. Figure 2 displays the low temperature (20 K) NIPE spectrum of the selected species obtained using 193 nm photons (photon energy 6.424 eV). A strikingly broad spectral profile with numerous

Table 1. Calculated adiabatic (ADEs) and vertical detachment energies (VDEs) for $[HFIP_{-H}\cdot HO_2]^-$ and $[HFA\cdot H_2O_2]^-$ complex anions at the DLPNO-CCSD(T)/aug-cc-pVTZ//ωB97XD/jun-cc-pVTZ level of theory

	Neutral-Singlet		Neutral-Triplet	
Anion	ADE/eV	VDE/eV	ADE/eV	VDE/eV
$[HFIP_{-H}\cdot HO_2]^-$				
A_1	3.35	4.15	2.13	3.17
A_2	3.16	5.48	1.93	4.78
$[HFA\cdot H_2O_2]^-$				
B_1	1.81	2.91	3.91	5.84
B_2	1.79	2.67	5.21	6.62

unresolved features ranging from 2.5 eV all the way up to electron binding energy (EBE) near the photon energy limit is unveiled. It should be noted that the relative intensity of two subregions, centered at 3.5 eV (labeled as I) and 4.8 eV (labeled as II), varies among the supplementary repetitive experiments, a fact strongly suggesting that multiple coexisting isomers contribute to the experimental spectrum with the isomeric populations fluctuated even under nearly identical conditions (more experimental data are available in Figure S1). Indeed, trapping and detecting multiple isomers within a few kilocalories per mole energy window were demonstrated in previous studies using the cold ion trap coupled with ambient ESI source.[31–33] Considering the broad spectral bands and overlapping spectral features, the experimental vertical detachment energies (VDEs) of different isomers can hardly be determined accurately from the spectral band maxima, whereas the adiabatic detachment energies (ADEs) corresponding to at least one of the detected isomers is estimated from the onset threshold to be 2.59 eV. In addition, a comparison to the previously reported spectra of $[HFA]^{\bullet -}$[34] and $[HFIP_{-H}]^-$[35] (see Figure S2) reveals that this spectral band bears no similarity to either spectrum, implying a completely different photoelectron detachment scenario. A detailed inspection of this recorded spectrum is therefore desirable.

Theoretical ADEs and VDEs are calculated based on the optimized structures in anionic and neutral charge states (Table 1) to preliminarily screen possible transitions. In the case of A_1, the theoretical ADEs/VDEs for transitions to the neutral in singlet and triplet states are 3.35/4.15 eV and 2.13/3.17 eV, respectively. The large VDE-ADE energy differences can be attributed to large structural changes induced by electron removal. Notably, there is a large singlet-triplet energy gap of 0.98 eV (VDE difference), reminiscent of the excitation energy of O_2 (0.98 eV)[36] from the lowest energy state $^3O_2$ to its first excited state $^1O_2$. The theoretical ADEs and VDEs of A_2 are determined to be 3.16/5.48 eV (singlet) and 1.93/4.78 eV (triplet), with significantly larger VDE-ADE energy differences than the values of A_1, indicating more pronounced geometric changes upon electron detachment, in line with a larger extent of proton transfer predicted for transitions in A_2. All theoretical detachment energies are within the energy range of the recorded spectral band, except for the two ADEs that correspond to accessing the two optimized neutral triplet complexes. The absence of such spectral signals is presumably due to negligible 0-0 transition intensities originating from considerably large anion-to-neutral geometry changes. Neither of the two isomers alone provides a satisfactory match to the experiment, strongly indicating both A_1 and A_2 present under the experimental conditions.

An opposite trend is observed for the B isomers, i.e., the calculated transition energies from the anion ground states to the singlet neutral states are significantly smaller than those analogs corresponding to the triplet neutral states. For instance, the VDE difference for transitions to the singlet and triplet states in B_1 is derived to be −2.93 eV. In the previous photoelectron spectroscopy study of the $HFA^{\bullet -}$ radical anion,[34] a similarly giant singlet-triplet splitting (−2.80 eV) was determined for HFA molecule, suggesting that the electron-emitting situation in B_1 is analogous to $HFA^{\bullet -}$. However, a closer examination of ADEs and VDEs precludes the dominant presence of configuration B, which would have otherwise resulted in an appreciable band gap in the EBE range of 3.0–5.0 eV, in contrast to the experimental observation.

In order to interpret the extremely broad band structures, Franck-Condon factor (FCF) simulations based on each specific transition from the anion ground state to the neutral singlet or triplet counterpart for all low-lying isomers were further conducted (Figure S3). The normal coordinate displacement vectors of predominant vibrational modes for each transition are displayed in Figure S4. The FCF simulated spectrum of A_1 for the transition to the triplet neutral state exhibits a complex vibrational pattern arising from multiple

excitations of different vibrational modes, including carbon skeleton vibrations, O-H wagging, and O-O bending vibrations. The excitations of low-frequency vibrational modes are congruous with the formation of HFIP (*SC*) in accompany of a departing O_2 moiety that results in producing a spectral band in EBE = 3.0–3.7 eV, yet significantly narrower than the observed spectrum. The simulation of A_1 for the transition to the singlet neutral state yields a prominent vibrational progression dominated by the O-O stretching mode. In the case of A_2, a long vibrational progression with a spacing of 470 meV associated with the O-H stretching is predicted for the transition to the triplet neutral state, consistent with the predicted proton transfer upon electron removal. Several low-frequency vibrations involving the HO_2-related rocking modes are active as well in consequence of the anion-to-neutral geometry change that occurs in a similar way of A_1. For the transition to the singlet neutral state, FCF simulation gives progressions with peak spacings of 470 and 210 meV, originating from the excitations of the O-H and O-O stretching modes.

For the $[HFA{\bullet}H_2O_2]^-$ configuration, the FCF simulated spectrum from B_1 transitioning to the singlet neutral state is not obtainable because of insignificant wavefunction overlaps between these two electronic states arising from substantial geometry changes in their equilibrium structures upon electron removal. Compared to the A isomers, the simulation of B_1 transitioning to the triplet neutral state shows a denser and structureless spectrum (see the right trace of Figure S3) with intense peaks involving the combination bands of the O-H stretching and bending modes. The transitions to singlet neutral state of B_2 possess appreciably weaker intensity in view of the large anion-to-neutral geometry change, with the rocking and wagging modes associated with H_2O_2 to be active, which is consistent with the displacement of H_2O_2 molecule as an entity moving around the oxygen atom of HFA moiety upon photodetachment. The main progression throughout the FC spectrum of B_2 transitioning to the triplet neutral state is derived from the O-H stretching mode, while other peaks with lower intensity are the combination bands involving excited quanta of the O-H bending and various low-frequency intermolecular vibrations. Apparently, a higher photon energy than 193 nm employed in this work is required to detect this transition.

Despite the aforementioned, extensive vibrational progression analyses, the complexity of the experimental spectrum with numerous fine peaks sitting on one broad band makes concrete spectral assignments a challenge. Based on the relative free energy argument, configuration A should make a larger contribution to the spectrum. As depicted in Figure 2, FC simulated transitions from A_1 cover EBE range from 3.0 to 4.5 eV, accounting for a major part of the low binding energy features. For the higher EBE regions (larger than 4.5 eV), the peaks are primarily assigned to photoelectrons arising from the A_2 transitions to its triplet and singlet neutral. The transition of B_2 to the singlet neutral state is also included to account for the weak signal around the band origin. The transitions derived from B_1 to its triplet neutral state may contribute to the signals around 6.0 eV as well and blend with spectral features associated with the transition of A_2 to singlet neutral state. Considering the rather poor signal-to-noise ratio near the photon energy limit and the expected minor population of configuration B, the contribution of this possible transition to spectral measurements is not weighed up for the sake of convenience of discussion. Overall, the simulated spectrum summed up from the multiple isomers, i.e., A_1 and A_2 transitions to their triplet and singlet neutral states as well as B_2 to its singlet state matches reasonably well with the general profile of the measured spectrum. This explicit spectral assignment substantiates the coexistence of multiple isomers and the dominant presence of configuration A in the experiments. Furthermore, by comparing the summed-up simulated spectrum with the experimental one, a qualitative estimate for the $^1O_2$ efficiency can be achieved. In general, the detachment cross-section for generating a singlet state is smaller compared to that for the corresponding triplet state based on spin multiplicity consideration. Figure 2 indicates roughly equal areas for the singlet and triplet signals which in turn suggest more than half of the generated O_2 is singlet oxygen, even though the absolute quantum yield is hard to evaluate.

Evidently, the electron signals with high intensity at EBE around 3.7 eV is not well described by the above FC simulations, therefore other accessible detachment channels should be considered. A two-photon process, where the first photon dissociates the anion complex and the second photon photodetaches the daughter anion, constitutes a viable explanation. Among all conceivable photofragment anions with positive electron affinity (EA), $[HFIP_{-H}]^-$ anion is much more promising than HO_2^-, as the EA of the former neutral was previously reported to be 3.43 eV,[35] significantly higher than the EA of the latter 1.089 eV.[37] Accordingly, the undefined photoelectron intensity around 3.7 eV is provisionally attributed to the contribution of the $[HFIP_{-H}]^-$ fragment anion originating from photodissociation of $[HFIP_{-H}{\bullet}HO_2]^-$ as manifested in Figure S5.

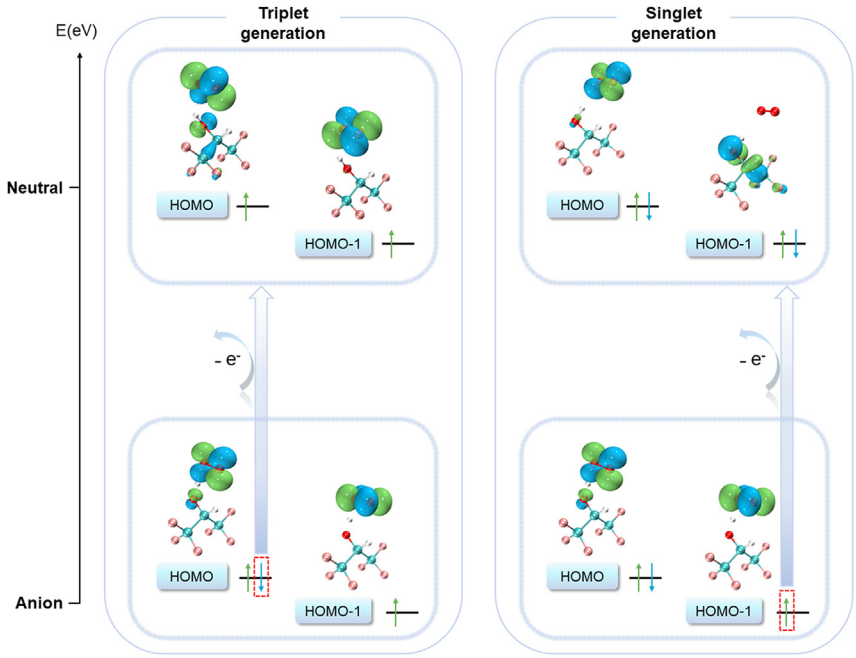

Figure 3. Frontier molecular orbital diagrams of A_1 anion complex and the corresponding detachment pathways leading to formations of the triplet and singlet neutrals.

To unravel the origins of detached electrons, calculations on the electronic structures of generated species are performed.[38] A comprehensive listing of molecular orbitals (MOs) for A_1 and corresponding neutrals are shown in Figure 3. The DFT results predict that the excess electron occupies one of the degenerated O_2 π_g* antibonding MOs, giving rise to the anion ground state with an electronic configuration consisting of a doubly occupied π_g MO (highest in energy, noted as HOMO in Figure 3) and a singly occupied π_g* MO (HOMO-1 with slightly lower energy). The O_2 doubly occupied π_g orbital orients toward the symmetry plane of $HFIP_{-H}$ moiety to augment the electron density along hydrogen bonding direction, leaving the singly occupied π_g* orbital perpendicular to the intermolecular interaction plane. In a simple one-electron transition picture, the produced triplet neutral complex corresponds to electron removal from the doubly occupied π_g orbital resulting in weakened hydrogen bonding interactions, qualitatively in agreement with the considerably elongated O_2•••HFIP distance by more than 1.0 Å upon photodetachment. In terms of generation of the singlet neutral complex, electron detachment from the singly occupied π_g* orbital induces less destabilization effects, supported by a smaller extent of structural rearrangement compared to that in transition to triplet neutral state. However, this description of detached electron originating from the configuration $(\pi_g^*)^1(\pi_g)^2$ can only be accepted within the single-determinant approximation. The violation of the lowest-energy electronic configuration predicted for the studied species evidently calls for the consideration of electron correlations.

Proposed photogeneration cycle for $^1O_2$ catalyzed by HFIP anion

From the perspective of geometries and electronic structures revealed by this spectroscopic study, a novel paradigm for the photogeneration of $^1O_2$ *in situ* via electron addition and photon irradiation in the UV optical range is hereby proposed. The formation of a negatively charged adduct $[HFIP•O_2]^-$ can be viewed as a consequence of proton transfer from HO_2 to $HFIP_{-H}$ moiety via strong hydrogen bonding interactions. As illustrated in Scheme 1A, the addition of a negative charge on the encounter complex HFIP•••$^3O_2$ results in a tightly bound anionic complex $[HFIP•O_2]^-$ with a dual intermolecular hydrogen bonding interaction consisting of one strong O–H•••O hydrogen bond and the other much weaker C–H•••O hydrogen bond. Following further exposure to UV irradiation on approach, a neutral complex is formed upon photoinduced detachment of the excess electron, producing an energetic molecular complex HFIP•••$^1O_2$ in an excited electronic state accessed by photons with sufficient energy. Being relatively longer-lived than isolated $^1O_2$ upon deactivations in practical reaction systems, this weakly interacting state facilitates the utilization of $^1O_2$ by increasing its lifetime and diffusion distance toward substrates. With the consumption of reactive $^1O_2$ from the protecting

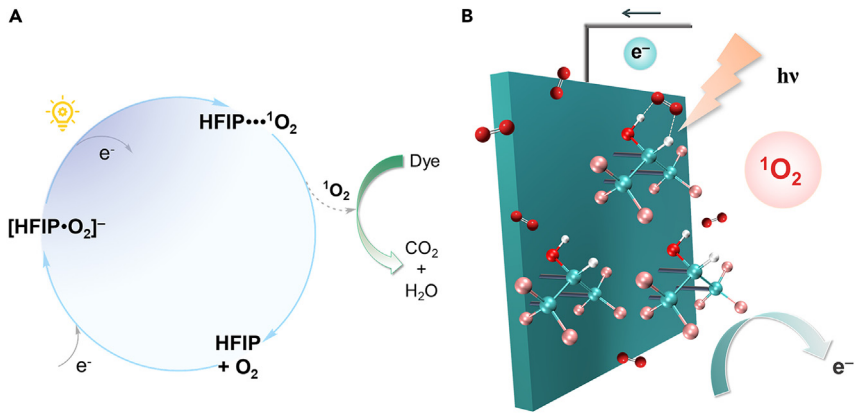

Scheme 1. Proposed photogeneration method for $^1O_2$

(A) The proposed photogeneration cycle for $^1O_2$ catalyzed by HFIP.

(B) a potential molecular assembly on the electrode surface for application to generate $^1O_2$ in wastewater purification devices.

reservoir, HFIP is resumed before binding the next O_2 molecule. Two proton translocation phases occur during the photogeneration cycle of $^1O_2$, one for each individual electron addition or removal step. This proposal can be in principle realized by the construction of a negative electrode functionalized with COOH-terminated self-assembled monolayers for immobilizing HFIP assembly via strong COOH•••F hydrogen bonds.[39] A precise control over electron transfer into the cathode coupled with the capture of dissolved oxygen provides access to critical intermediate $[HFIP•O_2]^-$, further enabling the release of reactive $^1O_2$ under photon irradiation. Overall, the critical element of the proposed mechanism is the controllable dye degradation efficiency in terms of photobleaching and following total elimination of significant organic residuals in the solution after decolorization by continuing the photogeneration cycle.

DISCUSSION

In conclusion, the NIPE spectrum of $[HFIP_{-H}•HO_2]^-$ anion complex in conjunction with supporting theoretical analyses offers new insights into the direct photogeneration of $^1O_2$ *in situ*. A hydrogen-bonded anionic complex $[HFIP•O_2]^-$ is assumed to be formed from a neutral adduct composed of HFIP molecule and gaseous O_2 upon electron introduction. The spectral assignment allows for the detection of produced $^1O_2$ weakly attached to HFIP with van der Waals interactions. The applied photons play a dual role in this optical excitation method, to be specific, generating $^1O_2$ by means of electron photodetachment and probing intriguing intermolecular interactions within anionic and neutral complexes. Importantly, successful regeneration of HFIP can be achieved after electron removal and release of $^1O_2$, rendering HFIP an effective "catalyst" in decolorization or mineralization cycle for dye contaminants. This work, therefore, provides a conceptually novel methodology for *in situ* generation of $^1O_2$ that is of merits to circumvent the troubled obstacles inherited from the current singlet oxygen sources and paves a new way to utilize $^1O_2$ for selective dye effluent degradation in an efficient and environment-friendly way.

Limitations of the study

Molecular mechanisms of a novel environment-friendly paradigm for photogeneration of reactive singlet oxygen catalyzed by HFIP for dye degradation are unraveled in this work. However, realization and demonstration of such novel methodology for practical use are still being actively pursued.

STAR★METHODS

Detailed methods are provided in the online version of this paper and include the following:

- KEY RESOURCES TABLE
- RESOURCE AVAILABILITY
  - Lead contact
  - Materials availability
  - Data and code availability

- METHOD DETAILS
  - Negative ion photoelectron spectroscopy
  - Computational details

SUPPLEMENTAL INFORMATION

Supplemental information can be found online at https://doi.org/10.1016/j.isci.2023.107306.

ACKNOWLEDGMENTS

This work was supported by the U.S. Department of Energy, Office of Science, Basic Energy Sciences, Chemical Sciences, Geosciences, and Biosciences Division, Condensed Phase and Interfacial Molecular Science program, FWP 16248, and performed using EMSL, a national scientific user facility sponsored by DOE's Office of Biological and Environmental Research and located at Pacific Northwest National Laboratory, which is operated by Battelle Memorial Institute for the DOE. The financial support of the National Natural Science Foundation of China (No. 21873089, 22073088) is gratefully acknowledged too. The quantum chemical calculations were performed on the supercomputing system in the Supercomputing Center of the University of Science and Technology of China.

AUTHOR CONTRIBUTIONS

J.H., Conceptualization, Methodology, Formal Analysis, Investigation and Writing – Original Draft. L.W., Conceptualization. W.C., and Q.Y., Investigation and Methodology. X.-B.W., X.Z. and S.L., Supervision, Writing – Review & Editing and Funding Acquisition.

DECLARATION OF INTERESTS

The authors declare no competing interests.

Received: February 27, 2023
Revised: May 3, 2023
Accepted: July 4, 2023
Published: July 10, 2023

REFERENCES

1. DeRosa, M., and Crutchley, R.J. (2002). Photosensitized Singlet Oxygen and Its Applications. Coord. Chem. Rev. *233–234*, 351–371.

2. Li, T., Ge, L., Peng, X., Wang, W., and Zhang, W. (2021). Enhanced Degradation of Sulfamethoxazole by A Novel Fenton-Like System with Significantly Reduced Consumption of H_2O_2 activated by g-C_3N_4/MgO composite. Water Res. *190*, 116777.

3. Bu, Y., Li, H., Yu, W., Pan, Y., Li, L., Wang, Y., Pu, L., Ding, J., Gao, G., and Pan, B. (2021). Peroxydisulfate Activation and Singlet Oxygen Generation by Oxygen Vacancy for Degradation of Contaminants. Environ. Sci. Technol. *55*, 2110–2120.

4. Gao, P., Tian, X., Nie, Y., Yang, C., Zhou, Z., and Wang, Y. (2019). Promoted Peroxymonosulfate Activation into Singlet Oxygen over Perovskite for Ofloxacin Degradation by Controlling the Oxygen Defect Concentration. Chem. Eng. J. *359*, 828–839.

5. Liu, S., Zhang, Z., Huang, F., Liu, Y., Feng, L., Jiang, J., Zhang, L., Qi, F., and Liu, C. (2021). Carbonized Polyaniline Activated Peroxymonosulfate (PMS) for Phenol Degradation: Role of PMS Adsorption and Singlet Oxygen Generation. Appl. Catal., B *286*, 119921.

6. Duan, X., Sun, H., Shao, Z., and Wang, S. (2018). Nonradical Reactions in Environmental Remediation Processes: Uncertainty and Challenges. Appl. Catal., B *224*, 973–982.

7. Peng, W., Dong, Y., Fu, Y., Wang, L., Li, Q., Liu, Y., Fan, Q., and Wang, Z. (2021). Non-Radical Reactions in Persulfate-Based Homogeneous Degradation Processes: A Review. Chem. Eng. J. *421*, 127818.

8. Lei, Y., Chen, C.-S., Ai, J., Lin, H., Huang, Y.-H., and Zhang, H. (2016). Selective Decolorization of Cationic Dyes by Peroxymonosulfate: Non-Radical Mechanism and Effect of Chloride. RSC Adv. *6*, 866–871.

9. Yang, Z., Qian, J., Yu, A., and Pan, B. (2019). Singlet Oxygen Mediated Iron-Based Fenton-Like Catalysis under Nanoconfinement. Proc. Natl. Acad. Sci. USA *116*, 6659–6664.

10. Zhu, S., Li, X., Kang, J., Duan, X., and Wang, S. (2019). Persulfate Activation on Crystallographic Manganese Oxides: Mechanism of Singlet Oxygen Evolution for Nonradical Selective Degradation of Aqueous Contaminants. Environ. Sci. Technol. *53*, 307–315.

11. Jawad, A., Zhan, K., Wang, H., Shahzad, A., Zeng, Z., Wang, J., Zhou, X., Ullah, H., Chen, Z., and Chen, Z. (2020). Tuning of Persulfate Activation from A Free Radical to A Nonradical Pathway through the Incorporation of Non-Redox Magnesium Oxide. Environ. Sci. Technol. *54*, 2476–2488.

12. Zhao, Y., Yu, L., Song, C., Chen, Z., Meng, F., and Song, M. (2022). Selective Degradation of Electron-Rich Organic Pollutants Induced by CuO@Biochar: The Key Role of Outer-Sphere Interaction and Singlet Oxygen. Environ. Sci. Technol. *56*, 10710–10720.

13. Wang, Z., Ai, L., Huang, Y., Zhang, J., Li, S., Chen, J., and Yang, F. (2017). Degradation of Azo Dye with Activated Peroxygens: When Zero-Valent Iron Meets Chloride. RSC Adv. *7*, 30941–30948.

14. Dong, J., Xu, W., Liu, S., Du, L., Chen, Q., Yang, T., Gong, Y., Li, M., Tan, X., and Liu, Y. (2021). Recent Advances in Applications of Nonradical Oxidation in Water Treatment: Mechanisms, Catalysts and Environmental Effects. J. Clean. Prod. *321*, 128781.

15. Chen, C., Wen, T., Liao, W., Gao, B., Jin, B., Dan, H., Li, Q., Yue, Q., Li, Y., Wang, Y., and

Xu, X. (2019). In-Situ Pyrolysis of Enteromorpha as Carbocatalyst for Catalytic Removal of Organic Contaminants: Considering the Intrinsic N/Fe in Enteromorpha and Non-Radical Reaction. Ann. Transl. Med. *7*, 382–395.

16. Brame, J., Long, M., Li, Q., and Alvarez, P. (2014). Trading Oxidation Power for Efficiency: Differential Inhibition of Photo-Generated Hydroxyl Radicals Versus Singlet Oxygen. Water Res. *60*, 259–266.

17. Tian, X., Gao, P., Nie, Y., Yang, C., Zhou, Z., Li, Y., and Wang, Y. (2017). A Novel Singlet Oxygen Involved Peroxymonosulfate Activation Mechanism for Degradation of Ofloxacin and Phenol in Water. Chem. Commun. *53*, 6589–6592.

18. Ding, Y., Wang, X., Fu, L., Peng, X., Pan, C., Mao, Q., Wang, C., and Yan, J. (2021). Nonradicals Induced Degradation of Organic Pollutants by Peroxydisulfate (PDS) and Peroxymonosulfate (PMS): Recent Advances and Perspective. Sci. Total Environ. *765*, 142794.

19. Zhu, S., Huang, X., Ma, F., Wang, L., Duan, X., and Wang, S. (2018). Catalytic Removal of Aqueous Contaminants on N-Doped Graphitic Biochars: Inherent Roles of Adsorption and Nonradical Mechanisms. Environ. Sci. Technol. *52*, 8649–8658.

20. Gao, Y., Chen, Z., Zhu, Y., Li, T., and Hu, C. (2020). New Insights into the Generation of Singlet Oxygen in the Metal-Free Peroxymonosulfate Activation Process: Important Role of Electron-Deficient Carbon Atoms. Environ. Sci. Technol. *54*, 1232–1241.

21. Kong, L., Fang, G., Xi, X., Wen, Y., Chen, Y., Xie, M., Zhu, F., Zhou, D., and Zhan, J. (2021). A Novel Peroxymonosulfate Activation Process by Periclase for Efficient Singlet Oxygen-Mediated Degradation of Organic Pollutants. Chem. Eng. J. *403*, 126445.

22. Waghchaure, R.H., Adole, V.A., and Jagdale, B.S. (2022). Photocatalytic Degradation of Methylene Blue, Rhodamine B, Methyl Orange and Eriochrome Black T Dyes by Modified ZnO Nanocatalysts: A Concise Review. Inorg. Chem. Commun. *143*, 109764.

23. Mapukata, S., Kobayashi, N., Kimura, M., and Nyokong, T. (2019). Asymmetrical and Symmetrical Zinc Phthalocyanine-Cobalt Ferrite Conjugates Embedded in Electrospun Fibers for Dual Photocatalytic Degradation of Azo Dyes: Methyl Orange and Orange G. J. Photochem. Photobiol., A *379*, 112–122.

24. Youssef, Z., Colombeau, L., Yesmurzayeva, N., Baros, F., Vanderesse, R., Hamieh, T., Toufaily, J., Frochot, C., Roques-Carmes, T., and Acherar, S. (2018). Dye-Sensitized Nanoparticles for Heterogeneous Photocatalysis: Cases Studies with TiO_2, ZnO, Fullerene and Graphene for Water Purification. Dyes Pigments *159*, 49–71.

25. Jańczyk, A., Krakowska, E., Stochel, G., and Macyk, W. (2006). Singlet Oxygen Photogeneration at Surface Modified Titanium Dioxide. J. Am. Chem. Soc. *128*, 15574–15575.

26. Dimitrijevic, N.M., Rozhkova, E., and Rajh, T. (2009). Dynamics of Localized Charges in Dopamine-Modified TiO_2 and their Effect on the Formation of Reactive Oxygen Species. J. Am. Chem. Soc. *131*, 2893–2899.

27. Han, F., Kambala, V.S.R., Srinivasan, M., Rajarathnam, D., and Naidu, R. (2009). Tailored Titanium Dioxide Photocatalysts for the Degradation of Organic Dyes in Wastewater Treatment: A Review. Appl. Catal., A *359*, 25–40.

28. Motiwala, H.F., Armaly, A.M., Cacioppo, J.G., Coombs, T.C., Koehn, K.R.K., Norwood, V.M., 4th, and Aubé, J. (2022). HFIP in Organic Synthesis. Chem. Rev. *122*, 12544–12747.

29. Colomer, I., Chamberlain, A.E.R., Haughey, M.B., and Donohoe, T.J. (2017). Hexafluoroisopropanol as A Highly Versatile Solvent. Nat. Rev. Chem *1*, 0088.

30. Bhattacharya, T., Ghosh, A., and Maiti, D. (2021). Hexafluoroisopropanol: The Magical Solvent for Pd-Catalyzed C–H Activation. Chem. Sci. *12*, 3857–3870.

31. Zhang, H., Cao, W., Yuan, Q., Zhou, X., Valiev, M., Kass, S.R., and Wang, X.-B. (2020). Cryogenic "Iodide-Tagging" Photoelectron Spectroscopy: A Sensitive Probe for Specific Binding Sites of Amino Acids. J. Phys. Chem. Lett. *11*, 4346–4352.

32. Han, J., Wang, L., Cao, W., Yuan, Q., Zhou, X., Liu, S., and Wang, X.-B. (2022). Manifesting Direction-Specific Complexation in $[HFIP_{-H}\cdot H_2O_2]^-$: Exclusive Formation of a High-Lying Conformation. J. Phys. Chem. Lett. *13*, 8607–8612.

33. Yuan, Q., Feng, W., Cao, W., Zhou, Y., Cheng, L., and Wang, X.-B. (2022). Sodium Cationization Enables Exotic Deprotonation Sites on Gaseous Mononucleotides. J. Phys. Chem. Lett. *13*, 9975–9982.

34. Wang, L., Han, J., Yuan, Q., Cao, W., Zhou, X., Liu, S., and Wang, X.-B. (2021). Electron Affinity and Electronic Structure of Hexafluoroacetone (HFA) Revealed by Photodetaching the $[HFA]^{\bullet-}$ Radical Anion. J. Phys. Chem. A *125*, 746–753.

35. Wang, L., Yuan, Q., Cao, W., Han, J., Zhou, X., Liu, S., and Wang, X.-B. (2020). Probing Orientation-Specific Charge–Dipole Interactions between Hexafluoroisopropanol and Halides: A Joint Photoelectron Spectroscopy and Theoretical Study. J. Phys. Chem. A *124*, 2036–2045.

36. Schweitzer, C., and Schmidt, R. (2003). Physical Mechanisms of Generation and Deactivation of Singlet Oxygen. Chem. Rev. *103*, 1685–1757.

37. Clifford, E.P., Wenthold, P.G., Gareyev, R., Lineberger, W.C., DePuy, C.H., Bierbaum, V.M., and Ellison, G.B. (1998). Photoelectron Spectroscopy, Gas Phase Acidity, and Thermochemistry of *tert*-Butyl Hydroperoxide: Mechanisms for the Rearrangement of Peroxyl Radicals. J. Chem. Phys. *109*, 10293–10310.

38. Lu, T., and Chen, F. (2012). Multiwfn: A Multifunctional Wavefunction Analyzer. J. Comput. Chem. *33*, 580–592.

39. Nakamura, F., Ito, E., Hayashi, T., and Hara, M. (2006). Fabrication of COOH-Terminated Self-Assembled Monolayers for DNA Sensors. Colloids Surf., A *284–285*, 495–498.

40. Yuan, Q., Cao, W., and Wang, X.B. (2020). Cryogenic and Temperature-Dependent Photoelectron Spectroscopy of Metal Complexes. Int. Rev. Phys. Chem. *39*, 83–108.

41. Lu, T.. Molclus Program. http://www.keinsci.com/research/molclus.html.

42. Bannwarth, C., Ehlert, S., and Grimme, S. (2019). GFN2-xTB-An Accurate and Broadly Parametrized Self-Consistent Tight-Binding Quantum Chemical Method with Multipole Electrostatics and Density-Dependent Dispersion Contributions. J. Chem. Theor. Comput. *15*, 1652–1671.

43. Chai, J.-D., and Head-Gordon, M. (2008). Long-Range Corrected Hybrid Density Functionals with Damped Atom–Atom Dispersion Corrections. Phys. Chem. Chem. Phys. *10*, 6615–6620.

44. Papajak, E., and Truhlar, D.G. (2011). Convergent Partially Augmented Basis Sets for Post-Hartree−Fock Calculations of Molecular Properties and Reaction Barrier Heights. J. Chem. Theor. Comput. *7*, 10–18.

45. Frisch, M.J., Trucks, G.W., Schlegel, H.B., Scuseria, G.E., Robb, M.A., Cheeseman, J.R., Scalmani, G., Barone, V., Petersson, G.A., Nakatsuji, H., et al. Gaussian 16 (Gaussian, Inc)

46. Riplinger, C., Pinski, P., Becker, U., Valeev, E.F., and Neese, F. (2016). Sparse Maps—A Systematic Infrastructure for Reduced-Scaling Electronic Structure Methods. II. Linear Scaling Domain Based Pair Natural Orbital Coupled Cluster Theory. J. Chem. Phys. *144*, 024109.

47. Dunning, T.H., Jr. (1989). Gaussian Basis Sets for Use in Correlated Molecular Calculations. I. The Atoms Boron through Neon and Hydrogen. J. Chem. Phys. *90*, 1007–1023.

48. Neese, F. (2012). The ORCA Program System. WIREs Comput. Mol. Sci. *2*, 73–78.

49. Gozem, S., and Krylov, A.I. (2022). The ezSpectra Suite: An Easy-to-Use Toolkit for Spectroscopy Modeling. Wiley Interdiscip. Rev. Comput. Mol. Sci. *12*, e1546.

50. Reimers, J.R. (2001). A Practical Method for the Use of Curvilinear Coordinates in Calculations of Normal-Mode-Projected Displacements and Duschinsky Rotation Matrices for Large Molecules. J. Chem. Phys. *115*, 9103–9109.

STAR★METHODS

KEY RESOURCES TABLE

REAGENT or RESOURCE	SOURCE	IDENTIFIER
Chemicals, peptides, and recombinant proteins		
Hexafluoroisopropanol	Sigma-Aldrich	CAS 920-66-1
Hydrogen peroxide	Sigma-Aldrich	CAS 7722-84-1
Methanol	Sigma-Aldrich	CAS 67-56-1
Software and algorithms		
Gaussian16	Frisch et al.[45]	https://gaussian.com
Genmer	Lu et al.[41]	http://www.keinsci.com/research/molclus.html
xtb	Grimme et al.[42]	https://github.com/grimme-lab/xtb
ORCA	Neese, F.[48]	https://orcaforum.kofo.mpg.de/app.php/portal
ezSpectrum	Gozem et al.[49]	https://iopenshell.usc.edu/downloads/

RESOURCE AVAILABILITY

Lead contact

Further information and requests for resources and reagents should be directed to and will be fulfilled by the lead contact, Prof. Xiaoguo Zhou (xzhou@ustc.edu.cn).

Materials availability

This study did not generate new unique reagent.

Data and code availability

- All data reported in this paper will be shared by the lead contact upon request.
- This paper does not report original code.
- Any additional information required to reanalyze the data reported in this paper is available from the lead contact upon request.

METHOD DETAILS

Negative ion photoelectron spectroscopy

The NIPES experiments were carried out using the Pacific Northwest National Laboratory magnetic–bottle time–of–flight (TOF) photoelectron spectrometer equipped with an ESI source and a temperature–controlled cryogenic ion trap.[40] The complex anion $[HFIP_{-H}{\bullet}HO_2]^-$ was produced by electrospraying an 1-mM aqueous methanolic (1:3 volume ratio) sample solution of HFIP at the pH value of 9–10 under H_2O_2 vapor. Similar procedures were used to produce $[HFIP_{-2H}]^{\bullet -}$ (namely $HFA^{\bullet -}$) radical anion, $[HFIP_{-H}]^-$ anion, and $[HFIP_{-H}{\bullet}H_2O_2]^-$ complex anion.[32,34,35] Accordingly, a second possible configuration with the same m/z of $[HFIP_{-H}{\bullet}HO_2]^-$ is proposed to be formed, i.e., $[HFA{\bullet}H_2O_2]^-$ complex anion. All anions were transported into vacuum by two RF–only ion–guides, accumulated and thermalized at 20 K in the ion trap. The cryogenically cooled anions were then pushed out at 10 Hz for mass-over-charge analyses in a TOF mass spectrometer. The anions of interest were carefully mass-selected and decelerated before being photodetached in the interaction zone with a 193 nm (6.424 eV) laser beam (EX100F, GAM ArF Laser). The laser was operated at a 20 Hz repetition rate with the anion beam off at alternating laser shots, enabling shot–by–shot background subtraction. The photodetached electrons were collected with nearly 100% efficiency by the magnetic–bottle and analyzed with a 5.2-m long electron flight tube. The recorded TOF photoelectron spectrum was converted into an electron kinetic energy spectrum, calibrated with the known transitions of I^- and $Cu(CN)_2^-$. The EBE spectrum presented in the paper was obtained by subtracting the kinetic energy spectrum from the detachment photon energy. The electron energy resolution was about 2% (i.e., ~20 meV for electrons with 1 eV kinetic energy).

Computational details

A large number of initial complex isomers were randomly generated using Genmer,[41] where configuration A is composed of $[HFIP_{-H}]^-$ anion and HO_2 radical, while configuration B comprises $[HFIP_{-2H}]^-$ anion and H_2O_2 molecule. Preliminary optimizations were performed with the semiempirical quantum mechanical method GFN2-xTB[42] and the resulting ensemble were classified and sorted in energy. After extensive exploring, low-energy isomers (within 10 kcal/mol) were screened out for further optimization and frequency analyses. Geometry optimizations and electronic structure calculations were performed using DFT at the ωB97XD[43]/jun-cc-pVTZ[44] level for complex anions in each configuration and for the corresponding electron-removed neutral counterparts. Subsequent vibrational frequency analysis was conducted at the same level to confirm that the true minima were found and to compute zero-point energies (ZPEs). All DFT calculations were carried out using the Gaussian 16 software package.[45] Using the optimized geometries, more accurate single point energies, DLPNO-CCSD(T)[46]/aug-cc-pVTZ[47]//ωB97XD/jun-cc-pVTZ were computed using the ORCA program suite.[48] The theoretical ADE was calculated as the energy difference between the corresponding neutral complex and the anion at each own optimized geometries including ZPE corrections, while the VDE was computed as the energy difference between the neutral and anion, both at the optimized anion structure.

Using obtained anion and neutral geometries, their vibrational frequencies, and normal mode vectors, FCFs for the electronic transition from the doublet anion ground state to the singlet and triplet states of the neutral were calculated using the ezSpectrum program,[49] including Duschinsky rotation.[50] Theoretical simulated spectra were consequently generated by broadening each FCF stick with experimental linewidth that can be directly compared to the experimental spectra.